I&EC research
Industrial & Engineering Chemistry Research

pubs.acs.org/IECR
Article

Aerographite vs Graphite: Investigating the Role of Electrode Architecture in H_2-Mediated Electroautotrophic Biofilms

Published as part of Industrial & Engineering Chemistry Research special issue "Smart Reactors - Towards Adaptive, Resilient, and Autonomous Process Systems".

Sri Sannihita Chavali, Christiane Roller, Tom Liebing, Jonas Lumma, Morten Möller, Rainer Adelung, Thorsten Alexander Kern, Miriam Edel, Bodo Fiedler, and Johannes Gescher*

Cite This: *Ind. Eng. Chem. Res.* 2026, 65, 17018−17029

ABSTRACT: Oxic microbial electrosynthesis using aerobic hydrogenotrophic bacteria requires productive cathodic biofilm formation, yet reactive oxygen species (ROS) generated at the electrode surface present a critical barrier to initial colonization. This study investigates biofilm development by *Cupriavidus necator* H16 on Aerographite, an ultralow-density carbon foam (3−12 mg cm^{-3}, porosity > 99%) with a hierarchical tetrapodal pore network, as a cathode material in microfluidic bioelectrochemical systems and compares it to graphite (a composite material consisting of graphite and polypropylene (PPG86)). A biphasic cultivation strategy, in which heterotrophic biofilm establishment preceded a switch to electroautotrophic conditions at −45.45 μA cm^{-2}, successfully overcame the ROS barrier on both electrode materials. Noninvasive optical coherence tomography revealed a final biovolume of 0.086 mm^3 mm^{-2} on graphite after 14 days, representing the first continuous kinetic characterization of *C. necator* cathode biofilm formation under defined flow conditions. Despite lower absolute biovolume per projected area, Aerographite supported higher biomass per unit electrode mass, reflecting its 585-fold higher mass-specific electroactive surface area relative to graphite. Scanning electron microscopy confirmed *C. necator* colonization of internal pore regions up to 500 μm below the electrode surface under laminar flow-over conditions. The macropore dimensions substantially exceed documented self-limiting biofilm thicknesses, indicating that pore occlusion is unlikely even at full biofilm development, and positioning Aerographite as a structurally enabling electrode material for smart, scalable, flow-through CO_2 valorization systems.

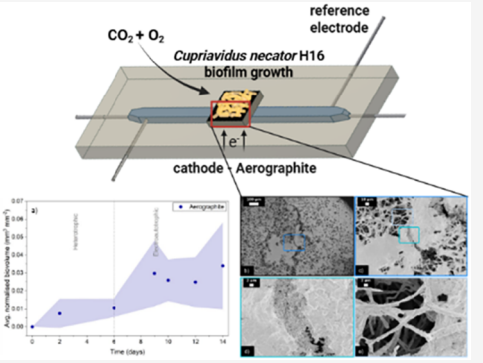

1. INTRODUCTION

Microbial electrosynthesis (MES) represents a sustainable platform for the electrochemical reduction of carbon dioxide into organic compounds by using microorganisms as biocatalysts that interact with cathodes as electron and energy donors.[1−4] This approach offers the benefit of using electricity as an increasingly sustainable and cost-effective electron donor. Furthermore, the operational voltage of such bioelectrochemical systems is significantly lower than that of typical water electrolyzers, potentially enabling higher biotechnological efficiency compared to two-step strategies where water electrolysis is followed by hydrogen-based fermentation. The potential for MES to compete with established biotechnological routes has recently been validated by Cabau-Peinado et al.,[5] who demonstrated that microbial electrosynthesis from carbon dioxide can reach space-time yields and productivities comparable to syngas and chain elongation fermentations. Hence, this study fundamentally challenged the perception that bioelectrochemical systems are inherently low-rate processes.

While conventional MES systems predominantly employ anaerobic microorganisms such as acetogens and methanogens, these biocatalysts face inherent limitations including restricted product spectra, low biomass yields due to energetic constraints, and the requirement for membrane-separated reactor configurations.[6] Oxic microbial electrosynthesis (OMES) has emerged as a promising alternative that utilizes aerobic, hydrogen-oxidizing bacteria as biocatalysts.[7−9] The highly exergonic nature of aerobic respiration provides these organisms with greater metabolic flexibility, enabling higher biomass accumulation rates and the potential for producing complex products such as proteins suitable for food and feed

Received: March 6, 2026
Revised: July 6, 2026
Accepted: July 21, 2026
Published: August 7, 2026

Table 1. Comparative Analysis of Physical, Electrical, and Biological Properties of 3D Carbon-Based Cathode Materials in Bioelectrochemical Systems (BES)

material	surface area (BET)	conductivity (S m^{-1})	surface area per volume (m^2/m^3)	porosity	microbial colonization (BES context)	sources
reticulated vitreous carbon (RVC)	~0.065 m^2 g^{-1}	~133	610−3900	90−97%	can be developed as an excellent 3D scaffold for deep biofilm growth by direct growth of carbon nanofibers on RVC or electrodeposition.	21−24
carbon felt	1.5−2.0 m^2 g^{-1}	0.9−800	9.8×10^3	90−99%	supports high initial power densities but prone to "bioclogging" and mass transport losses during long-term operation.	25−28
graphite granules	0.8−2.3 m^2 g^{-1}	~37.4	bed-dependent	bed-dependent	high stability for CO_2 reduction; performance limited by contact resistance between granules and potential mass transfer limits.	29,30

applications.[10,11] Additionally, OMES systems can operate without separating membranes between anode and cathode compartments, potentially reducing capital costs, while the in situ consumption of electrochemically generated hydrogen by the biofilm eliminates concerns about explosive gas mixtures that complicate conventional gas fermentation processes.[12] The thermoacidophilic knallgas bacterium *Kyrpidia spormannii* EA-1[3] has emerged as a particularly well-characterized model for OMES. After its identification as the first electroautotrophic cathodic biofilm biocatalyst of its kind,[3] the development of an OCT-based flow-cell methodology[13] enabled continuous, noninvasive kinetic monitoring of cathodic biofilm growth. Subsequent adaptive laboratory evolution of *K. spormannii* EA-1 yielded a 4-fold increase in biofilm accumulation rate and substratum coverage within ~ 3 days, with mean biofilm thicknesses on the order of 100 μm after 10 days.[14] More recent process-level analyses have shown that OMES with *K. spormannii* can achieve Coulombic efficiencies for CO_2 reduction to biomass of up to 28%, with nearly 100% biotic electron consumption when oxygen concentrations are carefully controlled to minimize abiotic losses at the cathode surface.[12] Under optimal process conditions, the solar energy demand for OMES-based biomass production was determined to be 67.89 kWh kg^{-1} dry biomass, which compares favorably to C_3 plants (324.07 kWh kg^{-1}), C_4 plants (138.89 kWh kg^{-1}), and microalgae cultivation in realistic outdoor reactors (111.11 kWh kg^{-1}).[12] This competitive energy efficiency is primarily attributed to the higher conversion efficiency of photovoltaic systems compared to photosynthesis when coupling solar energy capture with electrochemical hydrogen production.[15,16] Together, these studies have established a kinetic and quantitative reference framework specifically for *K. spormannii* cathode biofilms; whether the same framework applies to other aerobic hydrogenotrophs has so far not been examined.

While the bulk-phase availability of oxygen is a prerequisite for aerobic OMES, oxygen presents a localized challenge at the polarized cathode surface, where abiotic O_2 reduction generates reactive oxygen species (ROS) that impair initial microbial colonization.[14,17,18] This surface-localized challenge acts only on bare or sparsely colonized electrodes, and is progressively eliminated as the biofilm develops, since respiratory O_2 consumption by the biofilm depletes dissolved O_2 before it reaches the electrode interface. Establishing initial biofilm coverage is therefore a key engineering step for OMES, and is the rationale for the biphasic cultivation strategy applied in this work.

The transition from two-dimensional planar electrodes to three-dimensional architectures represents a prerequisite for increasing biocatalyst loading and achieving high current densities in MES systems. While traditional three-dimensional materials such as carbon felt and graphite granules have been extensively employed, they often suffer from pore clogging and restricted mass transfer. In these systems, metabolic by-products such as hydroxide ions produced during cathodic reduction accumulate within the matrix, creating inhibitory local pH gradients that stifle microbial activity.[19]

Despite significant progress in the development of three-dimensional cathode materials for microbial electrosynthesis (MES), most existing architectures involve trade-offs between surface area, pore accessibility, electrical conductivity, and mass transport. Dense fibrous or granular matrices (such as carbon felt and graphite granules) frequently promote biofilm overgrowth near the exterior surface while limiting nutrient diffusion and gas exchange within the interior volume. Consequently, the identification of electrode architectures that simultaneously support deep microbial colonization, efficient metabolite transport, and scalable electrochemical performance remains a central challenge in research. Table 1 summarizes representative three-dimensional electrode materials (reticulated vitreous carbon, carbon felt, and graphite granules) employed in MES and highlights the structural limitations that motivate the exploration of alternative scaffold designs such as Aerographite.[20]

To overcome these architectural constraints, we propose the use of Aerographite, a novel synthetic carbon foam characterized by a hierarchical network of seamlessly interconnected, hollow microtubes. Originally developed by Mecklenburg et al.,[31] Aerographite is synthesized via a sacrificial template method using Zinc oxide tetrapods, resulting in an ultralow-density material that is over 99.9% air. Its unique morphology provides a specific surface area that rivals graphene-based aerogels while maintaining superior mechanical elasticity and tunable electrical conductivity.[32,33] Highly porous and low-density carbon materials have garnered increasing research interest due to their outstanding and tailorable properties, including high porosities, large specific surface areas, electrical and thermal conductivity, and chemical inertness, making them suitable for diverse applications including energy storage, catalysis, sensing, and filtration.[34−38] Since the development of the first carbon aerogels in the late 1980s based on pyrolysis of resorcinol-formaldehyde organic aerogels,[39] this material class has expanded to include aerogels synthesized from carbon nanotubes[40−42] and graphene.[43−45]

In comparison to typical aerogels, Aerographite provides a structural hierarchy, which is beneficial for microbial colonization.[46] With typical pore windows ranging from 10 to 500 μm, the scaffold offers a habitable zone that significantly exceeds the dimensions of typical productive microbial biofilms. This disparity facilitates deep inward colonization and the development of a confluent biofilm on the material,

https://doi.org/10.1021/acs.iecr.6c01035
Ind. Eng. Chem. Res. 2026, 65, 17018−17029

while the open-pore network ensures nutrient flux and gas evolution. Consistent with the design principles for high-performance biointerfaces advocated by Jourdin & Burdyny.[47] Aerographite effectively decouples the available surface area from the reactor footprint.

In this study, we apply the metabolically versatile hydrogenotrophic bacterium *Cupriavidus necator* to investigate biofilm development on Aerographite surfaces. *C. necator* has been recognized as a key candidate for carbon dioxide-based biotechnology due to its thermodynamic flexibility as an aerobic hydrogenotrophic organism and its genetic tractability for producing platform chemicals.[48,49] Despite this strategic interest, kinetic information on *C. necator* cathode biofilms is scarce. The only direct study of *C. necator* at cathode surfaces to date was conducted by Bause et al.,[17] who reported end point SEM coverage of 34.8% on planar platinum after 24 h batch operation, but did not resolve biofilm development kinetics. Continuous, OCT-based kinetic data on *C. necator* cathode biofilms under defined flow conditions have therefore not previously been available and providing such data, in combination with a comparative assessment of Aerographite versus planar graphite as biofilm substratum, is the central aim of the present study.[13,48−50]

2. MATERIALS AND METHODS

2.1. Materials

All chemicals used in this study were of analytical grade and purchased from Carl Roth GmbH + Co. KG (Karlsruhe, Germany), Merck KGaA (Darmstadt, Germany) or Chemsolute Th. Geyer GmbH & Co. KG (Renningen, Germany). All gases were supplied by Westphalen AG (Hamburg, Germany). The Graphite electrodes used were a composite material consisting of graphite and polypropylene (PPG86) with an electrical conductivity of 60.15 S cm^{-2} and were purchased from Eisenhuth GmbH & Co. KG (Osterode am Harz, Germany).[50]

2.2. Synthesis and Characterization of Aerographite

2.2.1. Production of Tetrapodal ZnO Templates. The microscopic tetrapodal Zinc oxide (t-ZnO) template particles were synthesized via a flame transport synthesis method as reported elsewhere.[51,52] To obtain macroscopic templates with a defined geometry, loose powder consisting of t-ZnO particles was filled into a mold and compressed into the desired shape at a defined density. For the experiments conducted in this study, plates with a width and length of 6.8 cm, a height of 2.5 mm, and a density of 0.3 g cm^{-3} were produced. The plates were sintered at 1150 °C for 5 h to enhance the mechanical stability of the macroscopic templates through the formation of sinter bridges between the t-ZnO particles.[53] Subsequently, smaller templates with a length and width of 10 mm and a height of 2.5 mm were cut from larger plates using a CO_2 laser cutter. These templates were then used to produce Aerographite.

2.2.2. CVD-Synthesis of Aerographite. The Aerographite synthesis was based on a two-step process described by Mecklenburg et al.[31] In the chemical vapor deposition (CVD) synthesis, a Carbolite HZS 12/-900 tubular reactor was used. In the first synthesis step, the template morphology was replicated with carbon. The t-ZnO templates were placed on a silicon wafer on top of a quartz glass plate in the reactor. A schematic overview of the reactor is given in Figure 1.[54] The reactor was heated to a temperature of 760 °C; argon was flushed as an inert gas at a rate of 0.2 l min^{-1}. Once the reaction temperature was reached, hydrogen gas was supplied at a rate of 60 mL min^{-1} along with the carbon source, toluene, at a rate of 7 mL h^{-1}. All gases were preheated to 200 °C. After one hour, the toluene flow was stopped, and the reactor was heated to 900 °C and held at temperature for one hour for the reduction of ZnO. For cooling, the reactor was kept under an argon atmosphere with an increased flow of 0.4 l min^{-1}.

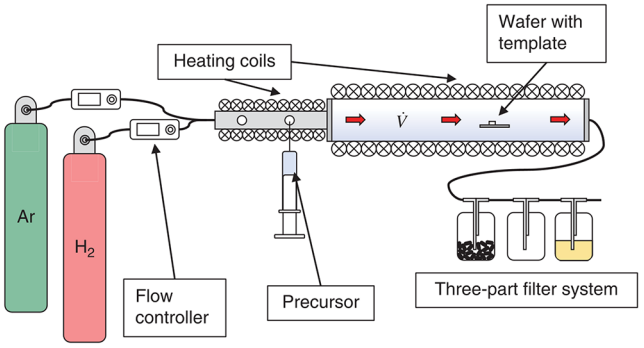

Figure 1. Schematic illustration of the CVD reactor.[54]

2.2.3. Determination of Density and Porosity. The determination of density and porosity of Aerographite was carried out by measuring the weight with a Sartorius CPA26P-0CE and the dimensions with calipers. For the dimensions, 5 measurements per value were taken, and the mean value was calculated, which was then used to calculate the density and porosity of the Aerographite.

2.2.4. Thermogravimetric Analysis. The ceramic residue was quantified with a Thermogravimetric Analysis (TGA; Thermal Analysis Q500). The TGA measurements were carried out under synthetic air flow, the sample was heated with a rate of 2 K min^{-1} to a maximum temperature of 900 °C.

2.2.5. Measurement of Electrical Conductivity. The electrical conductivity of Aerographite was determined by measuring the electrical resistance based on the method previously introduced by.[54] The gold-sputtered polyimide foils were replaced with copper sheets for improved contact. The Aerographite was placed between the copper sheets, and the measuring screw tightened until first contact of sample and copper was achieved. The electrical resistance was measured with a Keithley 2602 Sourcemeter in the four-wire setup. After the first contact with the sample the measurement screw was moved in one defined step closer to the sample and the resistance was determined. Ten samples were measured. From the resistance, sample height and area, the electrical conductivity was calculated, assuming areal contact between copper and Aerographite.

2.2.6. Electrochemical Characterization. Cyclic voltammetry (CV) and electrochemical impedance spectroscopy (EIS) were performed on both graphite and Aerographite electrodes in minimal medium[55] to characterize the electrochemical stability window and the interfacial charge transfer behavior. Cyclic voltammetry was conducted at a scan rate of 10 mV s^{-1} over a potential window of −1 to 1 V vs Ag/AgCl. EIS was performed at the open circuit potential with an AC perturbation amplitude of 10 mV. Initial measurements used a MultiEmStat4 potentiostat (PalmSens) over the frequency range 100 mHz to 100 kHz; measurements were subsequently extended on a Zürich Instruments MFIA impedance analyzer up to 5 MHz to resolve the high-frequency portion of the Nyquist response. The charge transfer resistance (R_{ct}) was extracted by fitting the Nyquist data to a Randles equivalent circuit using a geometric ellipse fit.

2.3. Reactor Design and Growth Conditions

2.3.1. Bioelectrochemical Setup. A scaled-down version of a bioelectrochemical system was established in microfluidic reactors as previously described, with required modifications to operate as a cathodic system.[50] Two reactors were used in series to house the three-electrode bioelectrochemical setup. The first reactor consisted of the working electrode (cathode) and the reference electrode custom-made with Ag/AgCl,[50] and the second consisted of the counter electrode (anode). These were separated into the cathodic and anodic compartments to facilitate gas supply to the cathodic compartment with predetermined gas atmosphere composition as described below. This system was used to compare the growth kinetics and material-microbe interaction between Aerographite and graphite and is represented in Figure 2. The electrodes were

https://doi.org/10.1021/acs.iecr.6c01035
Ind. Eng. Chem. Res. 2026, 65, 17018−17029

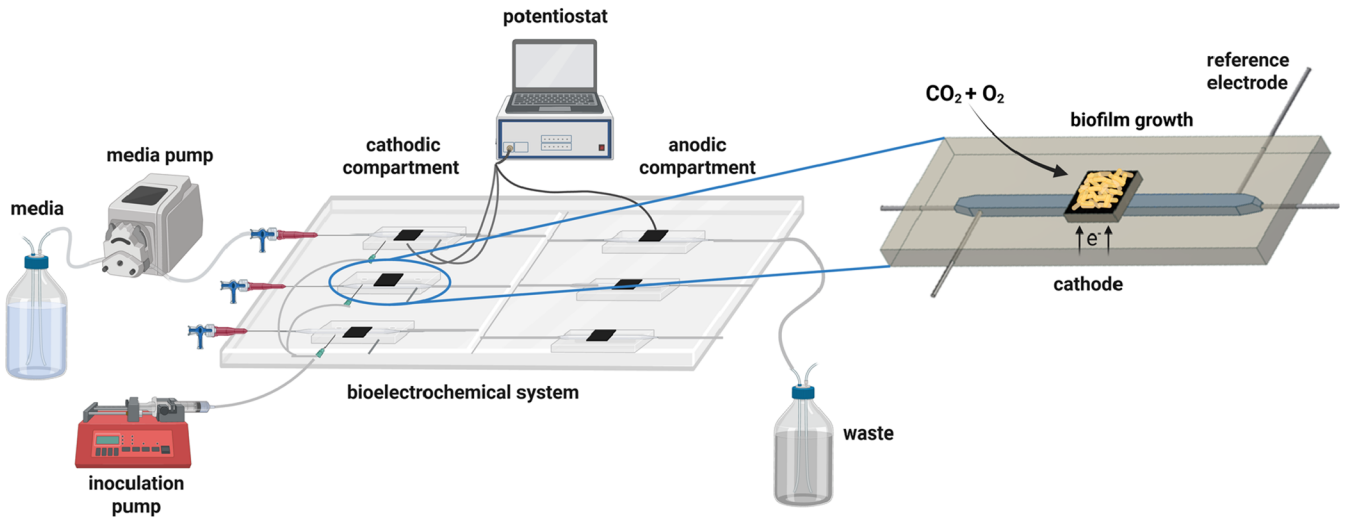

Figure 2. Schematic representation of a bioelectrochemical system with a closer look at the cathodic conversion process.

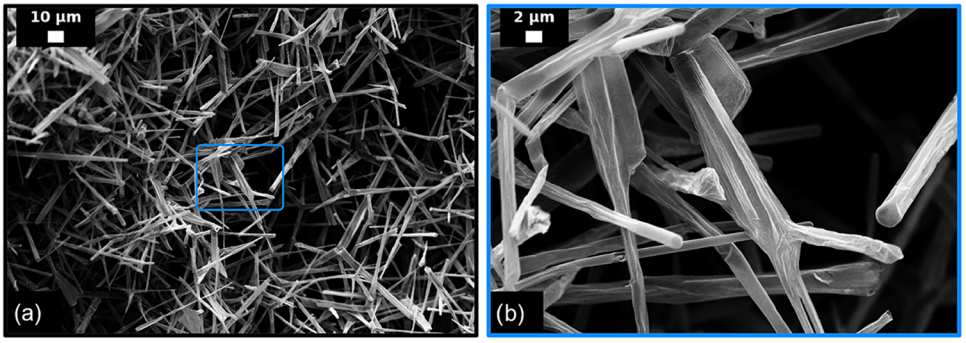

Figure 3. SEM image of Aerographite morphology before biofilm growth; sample has a density of 8.66 mg cm^{-3}, (a) overall morphology (b) gives the structure of individual tetrapod arms.

integrated into the microfluidic channel, ensuring a geometric working surface area ranging between 0.27 and 0.3 cm^2. The system was poised to −15 µA by connecting the bioelectrochemical setup to a potentiostat (Palmsens MultiEmStat4 LR) with the help of titanium foil (0.1 mm/99.6%; Chempure, Karlsruhe, Germany) connected to the cathode resulting in a current density of −45.45 µA cm^{-2}.

2.3.2. Strain and Growth Conditions. A *C. necator* H16 strain harboring a pBBR1 plasmid developed by Weiler et al.,[56] was used for all growth experiments in this work. The strain was precultivated in Lysogeny Broth with kanamycin (250 mg mL^{-1}) overnight at 30 °C and 180 rpm. The grown preculture was subsequently washed thrice in minimal medium[55] by centrifugation at 6000 rcf for 10 min each. The same media, with a pH of 6.8, was used for the microfluidic growth experiments. The inoculum was adjusted to a final optical density at 600 nm of 2.0 and supplemented with kanamycin (250 mg mL^{-1}) before introducing it into the cathodic bioelectrochemical reactor system. The inoculation process was carried out as described by Klein et al.[50]

2.3.3. Cultivation Strategy. All microfluidic growth experiments were conducted under identical electrochemical and hydrodynamic conditions for both graphite and Aerographite electrodes. Cathodic polarization at −45.45 µA cm^{-2} (corresponding to −15 µA over the geometric working area of 0.3 cm^2) was applied continuously from the moment of inoculation (day 0) until the end of the experiment (day 14). This polarization resulted in the electrodes being poised at a combined average potential of −0.67 ± 0.045 V in case of Graphite and −0.54 ± 0.05 V for Aerographite. The temperature was held at 30 °C and the medium flow rate, reactor geometry, and inoculation procedure were identical across all conditions. As discussed in the introduction, direct cathodic colonization under electroautotrophic conditions is hampered by abiotic reactive oxygen species (ROS) generated at the polarized electrode surface. To overcome this, a biphasic cultivation strategy was applied identically to both electrode materials. The two phases differed exclusively in carbon source not in electrical regime. In a heterotrophic start-up phase (day 0 to day 6) the medium contained fructose as organic carbon source, to establish rapid heterotrophic growth and a thin confluent biofilm on the cathode. In the subsequent electroautotrophic phase (day 6 to day 14) the medium was switched to a fructose-free formulation. In both phases we continuously flushed the cathode compartment with gas mixture composition (vol%): N_2: 80%; O_2: 15%; CO_2: 5%. To reduce ROS formation and increase primary production, oxygen concentration was reduced while carbon dioxide concentration was increased relative to air.

Control growth experiments were additionally performed for both graphite and Aerographite under nonpolarized conditions, with biofilm growth occurring at open-circuit potential rather than under an applied current. These control experiments confirm that the biovolume observed at −45.45 µA cm^{-2} can be attributed to electroautotrophic growth.

2.4. Analytical Methods

2.4.1. Optical Coherence Tomography (OCT). OCT was used to monitor the structure of biofilms using the Ganymede Series SD-OCT Systems from Thorlabs GmbH, Dachau, Germany. This provides a micrometre scale resolution of depth resolved images while being noninvasive. The image acquisition and data processing was carried out as described in Klein et al.[50] Due to the porous nature of the Aerographite electrode, the biovolume is estimated by calculating the total amount of voxels of biomass after accounting for the voxels representing the electrode top-surface.

https://doi.org/10.1021/acs.iecr.6c01035
Ind. Eng. Chem. Res. 2026, 65, 17018−17029

2.4.2. Scanning Electron Microscopy. To analyze the morphology of Aerographite electrodes before and after biofilm growth, a scanning electron microscope (SEM; Zeiss Supra VP 55, 3 kV acceleration voltage) at the Electron Microscopy Unit (BeEM) at the Hamburg University of Technology (TUHH) was used. At the end of the microfluidic growth experiments, the biofilm was fixed onto the electrodes using 4% glutaraldehyde (EM garde) for 24 h followed by washing with phosphate buffered saline, and an alcohol series (50, 70, 90 and 100%) for 20 min each. The electrodes were then cut out of the reactors and dried under ambient conditions before mounting them for SEM imaging. For better conductivity, the samples were sputtered with gold for 45 s at a voltage of 40 mA.[57]

3. RESULTS AND DISCUSSION

3.1. Morphology and Electrode Properties

Representative for the specific morphology a plain Aerographite with a density of 8.66 mg cm^{-3} and porosity of 99.62% was investigated with the SEM Figure 3a gives an overview of the three-dimensional interconnected network of the foam like structure, as well as the high porosity and low density of Aerographite. In Figure 3b, the tetrapods display a diameter of about 1−5 μm and a high wall thickness. This is indicated by the surface of the tetrapods which is partially smooth but also shows wrinkling in some parts. The ends of the tetrapods are fully closed. These observations are similar to the morphologies reported by Garlof and Mecklenburg et al.[31,33]

The TGA analysis was used to determine the ZnO residue in the Aerographite and thermal degradation temperature for both electrode materials. The difference in initial mass used for the analysis has no influence on the overall thermal properties recorded, since the device sensitivity is 0.1 μg. Results are shown in Figure 4. The graphite electrode shows an initial loss

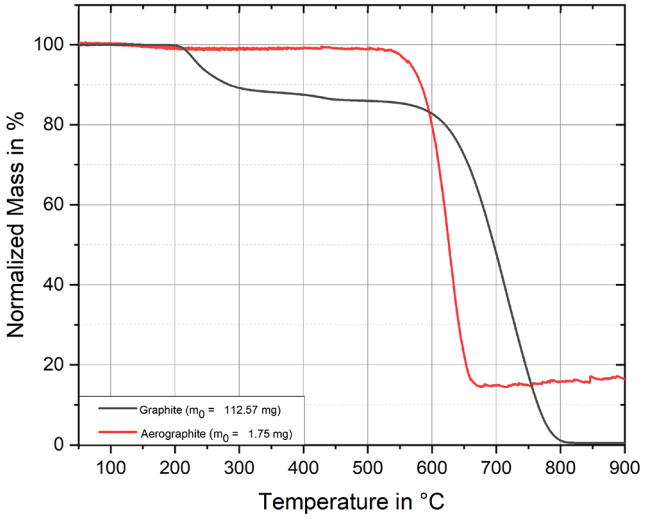

Figure 4. TGA spectra of Graphite and Aerographite Electrode.

of mass of 15% at 210 °C concluding at 460 °C, which is attributed to the polypropylene (PPG86)[58] fraction of the material composition. The second step of degradation takes place between 600 to 800 °C to a full decomposition of the electrode. This temperature range and single step decomposition are typical for graphitic carbon.[59,60] In Aerographite, however, the thermal degradation starts at 550 °C and is more rapid in comparison to the graphite electrode. The decreased ignition temperature indicates the transition state of the amorphous carbon as well as a lower average particle size of the graphite layers that make up the Aerographite tetrapods when compared to the Graphite electrode.[31,60] Additionally shown is that the degradation stops at 670 °C and a residue of 15% remains. This residue can be attributed to ZnO left over after the synthesis, which was not fully reduced.

3.2. Electrochemical Properties of Electrode Materials

3.2.1. Electrical Conductivity. For ten Aerographite samples from the same synthesis batch, electrical conductivity was measured as a critical material property to assess suitability for bioelectrochemical applications, where efficient electron transfer between electrode and biofilm is essential. Conductivity values were determined and plotted against sample density (Figure 5). The mean conductivity was 0.31 ± 0.08 S

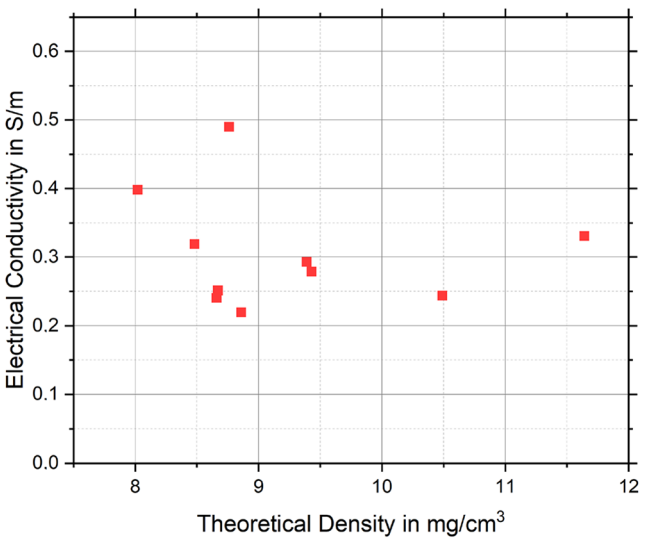

Figure 5. Electrical Conductivity of the Aerographite plotted against the theoretical density.

m^{-1} while being on the lower end, still comparable to the conductivity values measured before by Garlof et al.[32] (0.15−10.2 S m^{-1}). Not surprisingly, graphite electrodes showed a significantly higher conductivity of 1852.62 S m^{-1}.[50] The determined densities correspond to a thin-walled, closed-shell structure, and the conductivity reflects the characteristic hollow tetrapodal framework of Aerographite observed in earlier studies by Garlof et al.[32]

Although the bulk conductivity of Aerographite is several orders of magnitude lower than that of the graphite composite electrode (0.31 vs 1853 S m^{-1}), this difference reflects the >99% porosity of the material rather than the intrinsic conductivity of the CVD-derived graphitic carbon constituting the tetrapod walls. The relevant question for bioelectrochemical operation is therefore the ohmic voltage drop across the electrode under the applied current, rather than the bulk conductivity in absolute terms. At the operating current density of −45.45 μA cm^{-2} and the geometric electrode dimensions used here (0.3 cm^2 projected area, 2.5 mm thickness), the calculated ohmic drop through the Aerographite scaffold is on the order of 4 mV, which is negligible compared to the cathodic overpotentials required for hydrogen evolution and to typical performance differences observed between cathode materials in OMES. The low bulk conductivity of Aerographite is therefore not expected to limit performance in the present microfluidic configuration. At

https://doi.org/10.1021/acs.iecr.6c01035
Ind. Eng. Chem. Res. 2026, 65, 17018−17029

substantially larger electrode dimensions or significantly higher operating current densities, however, ohmic losses through low-conductivity 3D scaffolds will scale linearly with thickness and inversely with conductivity and would need to be balanced against the gains in biocatalyst loading provided by the macroporous architecture. The introduction of metallic current distributers in relevant distance could be a strategy to solve this problem.

To experimentally verify that the low bulk conductivity of Aerographite does not translate into an electrochemically meaningful interfacial limitation, electrochemical impedance spectroscopy was performed on both materials in the cell configuration used for biological experiments (Figure 6).

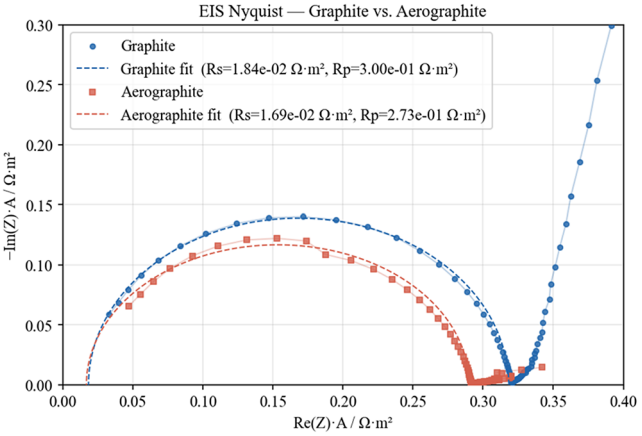

Figure 6. Nyquist plots of Aerographite (orange squares) and graphite (blue circles) electrodes. The spectra were recorded in Sydow media (same as is used in the bioelectrochemical growth experiments). The measurements were performed at open circuit potential with an AC perturbation amplitude of 10 mV. Data were collected using a MultiEmStat4 potentiostat (100 mHz to 100 kHz) and extended using a Zürich Instruments MFIA impedance analyzer up to 5 MHz to resolve the high-frequency response. Charge transfer resistance (R_{ct}) values were determined by fitting the data to a Randles equivalent circuit using a geometric ellipse fit.

Measurements over the frequency range 100 mHz to 100 kHz on a MultiEmStat4 potentiostat yielded high-frequency real-axis intercepts of 0.318 Ω·m^2 for graphite and 0.290 Ω·m^2 for Aerographite, but the capacitive arc did not fully close within this frequency window, precluding reliable extraction of the charge transfer resistance. Extending the measurement range to 5 MHz on a Zürich Instruments MFIA impedance analyzer resolved the full depressed semicircle for both electrodes. A Randles equivalent circuit fit yielded charge transfer resistances of R_{ct} = 0.300 Ω·m^2 for graphite and R_{ct} = 0.273 Ω·m^2 for Aerographite, with depression coefficients of 0.927 and 0.855 respectively, indicating only minor deviation from ideal semicircular behavior. Despite the ∼6000-fold difference in bulk conductivity between the two materials, the interfacial charge transfer resistance of Aerographite is therefore comparable to that of the graphite composite electrode.

3.2.2. Electroactive Surface Area (ESA). The microfluidic bioelectrochemical screening platform was structured in a manner that provides a fixed geometric surface area of 0.3 cm^2 over which the electrochemical reaction occurs facilitating biofilm growth. However, the porosity of the Aerographite was hypothesized to result in a lower electroactive surface area compared to a plain graphite surface.[61] To electrochemically evaluate the electroactive surface area, cyclic voltammetry (CV) peak current measurements (Figure 7) were conducted following the protocol established by.[61] The electrochemical tests were performed using the three-electrode microfluidic flow cell configuration detailed previously, with an electrolyte composed of 5 mM $K_4[Fe(CN)_6]$ dissolved in a 1 M aqueous KOH solution.

Given the complex architecture of the porous 3D Aerographite, an extended cyclic voltammetry window of −1.0 to +1.0 V vs Ag/AgCl was employed to establish the baseline electrochemical working window. Unlike planar surfaces, 3D porous matrices generate substantial nonfaradaic double-layer charging currents and can exhibit shifted onset potentials for water electrolysis due to local microenvironmental effects.[62,63] Scanning this broad potential range was therefore necessary to accurately map the capacitive background and confirm the solvent stability limits. This ensured that the peak currents (I_p) extracted for the Randles-Sevcik analysis of the $[Fe(CN)_6]^{3-}/[Fe(CN)_6]^{4-}$ probe were fully decoupled from any interfering background faradaic or pseudocapacitive processes originating from the electrode structure.

As described by the Randles-Sevcik equation (Formula 1), the peak current exhibits a direct proportionality to the electroactive surface area of the working electrode:

$$I_p = 268600 n^{(3/2)} A D^{(1/2)} C \nu^{(1/2)} \quad (1)$$

In this expression, I_p (A) represents the peak current, n is the number of electrons transferred during the redox reaction (equal to 1 here), and A (cm^2) is the electroactive surface area. The variable D (cm^2 s^{-1}) denotes the diffusion coefficient, which is 6 × 10^{-6} for $[Fe(CN)_6]^{4-}$, while C (mol cm^{-3}) represents the concentration of the active redox species, corresponding to 5 × 10^{-6} for $[Fe(CN)_6]^{4-}$. Finally, the scan rate is represented by v (V s^{-1}). Voltametric scans were executed at a rate of 0.01 V s^{-1}.

Thus, using the reductive peak current for the cathodic system, the electroactive surface area was calculated. The ESA for each corresponding sample along with other physical properties are shown in Table 2.

The average mass-specific ESA of Aerographite was 0.31 cm^2 mg^{-1}, compared to only 0.00053 cm^2 mg^{-1} for solid graphite,[61] representing a 585-fold increase. This enhancement is attributed to the ultralow density and hierarchical porosity of Aerographite, which exposes substantially more electrode surface per weight to the electrolyte than a dense graphite structure. The finding that the measured ESA (∼0.3 cm^2) closely matches the geometric cross-sectional area may appear surprising, given the large porosity of the material. it demonstrates that the electrochemical reaction is restricted to a very thin, 2D planar boundary layer on the outer surface of the highly porous electrode, indicating a highly diffusion-limited penetration depth. Following the transport principles outlined in[64] which addresses mass and charge transport limitations in porous 3D electrodes, we can model the active penetration depth (L_p) of our limiting cathodic reactant (dissolved electron acceptor CO_2/O_2 or proton/buffer species) using a simplified reaction-diffusion equation derived from Fick's second law:

$$D_{eff} \frac{d^2C}{dz^2} - r_{vol} = 0 \quad (2)$$

https://doi.org/10.1021/acs.iecr.6c01035
Ind. Eng. Chem. Res. 2026, 65, 17018−17029

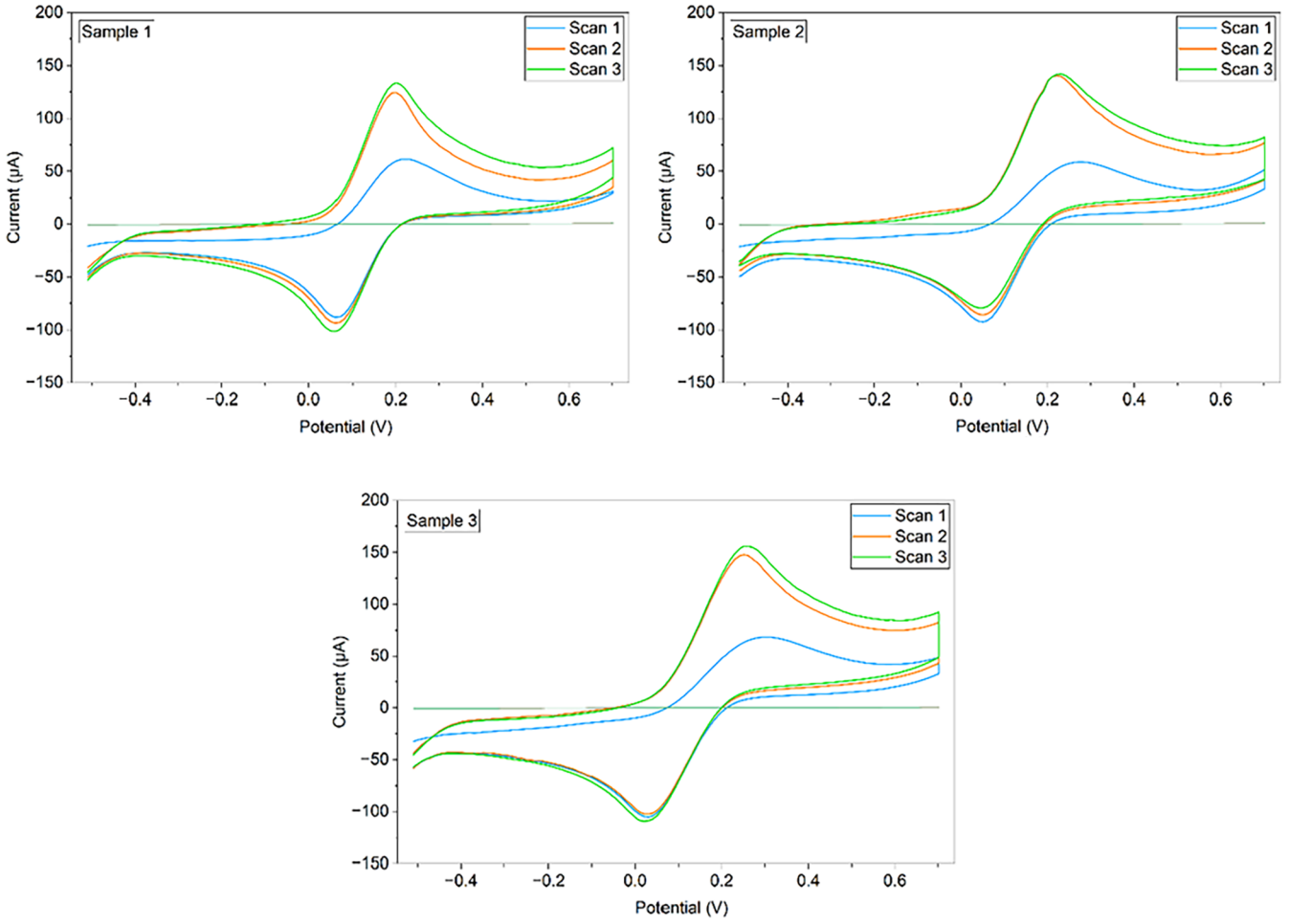

Figure 7. Cyclic voltammograms of Aerographite electrodes (Samples 1, 2, and 3) recorded in 5 mM $K_4[Fe(CN)_6]$ dissolved in a 1 M aqueous KOH solution as electrolyte. While the full experimental scans were conducted over a wider potential window (−1.0 to + 1.0 V vs Ag/AgCl) to establish baseline stability, the axes here are restricted to the −0.5 to + 0.7 V range to highlight the $[Fe(CN)_6]^{3-}/[Fe(CN)_6]^{4-}$ redox peaks. The cathodic peak currents extracted from these curves were used to calculate the electroactive surface area (ESA) values presented in Table 2.

Table 2. Correlation of Physical vs Electrochemical Properties of Aerographite

sample	density [mg cm^{-3}]	electroactive surface area [cm^2]	geometric surface area [cm^2]	ESA/mass [cm^2 mg^{-1}]
1	3.1	0.26 ± 0.02	0.33	0.34
2	5.5	0.29 ± 0.02	0.30	0.24
3	4.1	0.32 ± 0.01	0.32	0.35

Integrating this across the boundary of the porous matrix yields the characteristic penetration depth (L_p):

$$L_p = \sqrt{\frac{2 \cdot D_{\text{eff}} \cdot C_{\text{bulk}}}{r_{\text{vol}}}} \quad (3)$$

Where D_{eff} is the effective diffusion coefficient of the limiting substrate within the stagnant boundary layer of the porous electrode (approximated as 1.2×10^{-5} cm^2 s^{-1} to 1.9×10^{-5} cm^2 s^{-1} in water/biofilm matrix); C_{bulk} is the bulk concentration of the reactant/buffer; and r_{vol} is the volumetric consumption rate of the reactant by the electrotrophic biofilm.

Because the local metabolic consumption rate (r_{vol}) is high relative to slow, unassisted diffusion (D_{eff}) through the stagnant liquid within the uncompressed 3D electrode, the calculated penetration depth (L_p) is extremely small, in the order of 10 to 50 μm.

This mathematically explains why the deeper internal surfaces of our >99% porous electrode remain electrochemically inactive, restricting the active double-layer charging and redox reactions strictly to the outer geometric boundary.

Nevertheless, the total available surface area is far larger than the measured ESA. From SEM image analysis (Figure 10f), tetrapod arm lengths of 16 ± 9 μm (n = 600,[65]) and average diameters of 2 μm were determined (n = 30;[32]). Assuming hollow tubular arms with a typical wall thickness of 25 nm (characteristic of CVD-derived Aerographite,[66]), the total geometric surface area of the electrodes was estimated at approximately 125 cm^2. This implies that less than 0.3% of the total Aerographite surface is electrochemically accessible under the given conditions, most likely due to diffusion limitations within the porous network under laminar flow.

The observation that the majority of the Aerographite surface remains electrochemically inaccessible in the flow-over configuration is consistent with findings for other porous 3D electrode materials. Harrington et al.[67] demonstrated that in bioelectrochemical systems employing graphite felt electrodes with a specific surface area of approximately 61,600 m^2 m^{-3}, substantial electrode surface remained uncolonized even after steady-state current was reached. Similarly, Sleutels et al.[64]

https://doi.org/10.1021/acs.iecr.6c01035
Ind. Eng. Chem. Res. 2026, 65, 17018−17029

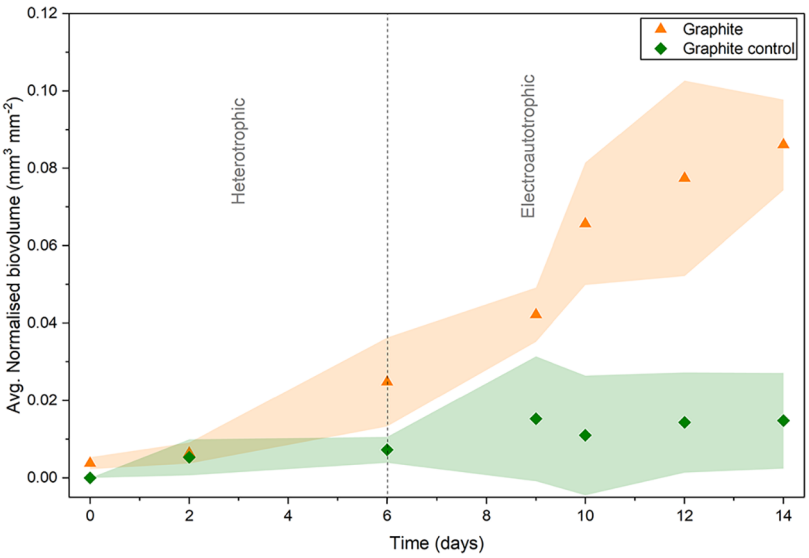

Figure 8. Biofilm development by *C. necator* on graphite electrodes under biphasic growth conditions, compared to a negative control at open circuit potential. Data represent the average of triplicates, with the shaded regions depicting the standard deviation. Growth on polarized electrodes is shown in orange, while control experiments on unpolarized electrodes are shown in green.

showed that forced convective flow through porous graphite felt anodes improved the transport of protons, buffer species, and substrates, leading to increased current densities compared to stagnant or flow-over configurations. Transition from flow-over to flow-through operation is therefore expected to substantially increase the fraction of the 125 cm^2 total Aerographite surface that participates in electrochemical turnover, by replacing diffusion-limited internal mass transport with convective supply. The macroscopic pore dimensions are a key structural advantage of Aerographite over conventional porous electrode materials such as carbon felt or graphite foam. While carbon felt typically exhibits pore sizes in the range of 10−50 μm, the open tetrapodal network of Aerographite provides pore spaces in the ranges of 10−500 μm. This large and highly interconnected porosity will have important implications for the long-term operability of flow-through configurations in bioelectrochemical systems.

Electroactive biofilms on electrode surfaces in bioelectrochemical systems typically reach self-limiting thicknesses governed by mass transfer constraints, with reported values of 100−150 μm for anodic mixed-species biofilms in microbial electrolysis cells[68] and 130−150 μm for cathodic *K. spormannii* biofilms.[12] These limits are not a universal property but emerge from the interplay of substrate diffusion (H_2, CO_2, O_2), product and proton accumulation, EPS density, shear stress, and intrinsic organism characteristics such as growth rate and EPS production. The specific value applicable to a given system therefore depends on the colonizing species, electrode morphology, and operating regime. For example, while both *K. spormannii* and *C. necator* are hydrogen-oxidizing autotrophs, they occupy opposite ends of this physiological spectrum. *K. spormannii* is a Gram-positive thermophile (optimal growth ∼55−60 °C) that naturally secretes a dense extracellular matrix to form robust cathodic biofilms.[69] Conversely, *C. necator* is a Gram-negative mesophile (∼30 °C) that favors a planktonic lifestyle, typically forming thinner, fragile biofilms.[70,71] Besides the individual biology driven properties of biofilm chemistry and architecture, the different temperature optima will certainly affect diffusion coefficients, solubility, but also cellular hydrogen oxidation rates. Therefore, the mentioned literature values are not universal thresholds but rather order-of-magnitude references.

Nevertheless, a substantial fraction of the macropore dimensions of Aerographite (10−500 μm) will likely be at or above the upper end of reported self-limiting cathodic biofilm thicknesses, suggesting that the macroporous architecture can structurally accommodate fully developed biofilms without complete pore occlusion in the larger pore fraction. Smaller pores in the lower end of the size distribution (10−50 μm) may be more susceptible to bridging or occlusion at high biofilm coverage, and this is an aspect that will need to be addressed in future flow-through studies.[12,68]

A second limitation associated with three-dimensional electrode architectures concerns the accumulation of hydroxide ions and the resulting local pH gradients within the porous matrix, which have been shown to inhibit microbial activity in packed-bed MES reactors operating at high current densities.[19] The relevance of this effect to the present configuration is, however, expected to be limited. The cathodic current density applied here (−0.45 A m^{-2}) is approximately one to 2 orders of magnitude lower than those typically reported, resulting in a correspondingly reduced local hydroxide production rate. Still, future upscaling studies will have to reveal whether the larger pore size together with higher flow rates and buffering of the medium will help to overcome these limitations during flow through operation even if higher current densities are applied.

3.3. Quantitative Evaluation of Cathodic Biofilm Growth of *C. necator* on Graphite Electrodes

In the OMES system investigated here, cellular biomass is the direct product of microbial electrosynthesis. Quantification of biovolume accumulation under electroautotrophic conditions therefore serves as a direct readout of electrosynthesis activity, provided that current-dependent growth can be separated from residual heterotrophic or carry-over growth. As outlined in the introduction, kinetic data on *C. necator* cathode biofilms under defined flow conditions have not previously been available; we therefore began by assessing this strain on plain graphite electrodes, including a parallel open-circuit potential (OCP)

https://doi.org/10.1021/acs.iecr.6c01035
Ind. Eng. Chem. Res. 2026, 65, 17018−17029

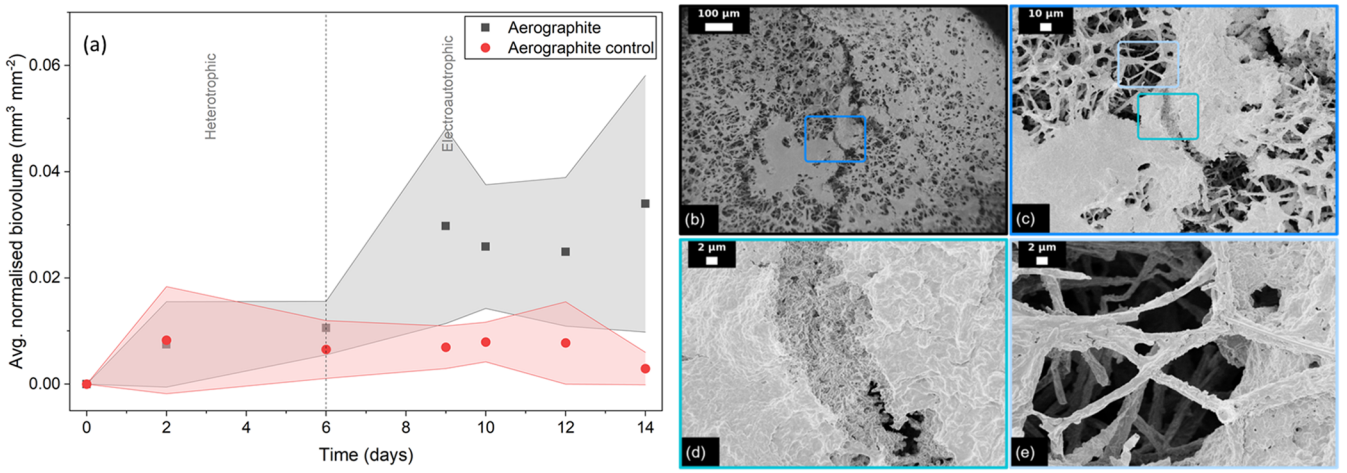

Figure 9. (a) Biovolume development by *C. necator* on Aerographite electrodes. Growth on polarized electrodes is shown in gray, while control experiments on unpolarized electrodes are shown in red. Fructose was fed for the first six days, after which growth occurred autotrophically. Data represent the average of triplicates, with the shaded region depicting the standard deviation. (b–e) Scanning electron micrographs of *C. necator* biofilm on Aerographite electrodes: (b) Electrode top surface after biofilm growth (c) Porous electrode structure with fully covered biofilm regions; (d) Surface-grown biofilm exhibiting distinct cell patches and extracellular material across the electrode; (e) Formation of biofilm stretching between tetrapodal network.

control to establish the baseline for current-dependent biofilm formation. Initial attempts to cultivate the strain directly under electroautotrophic conditions failed, which was attributed to the formation of reactive oxygen species (ROS) at the cathode surface due to abiotic oxygen reduction. Studies have identified ROS as a critical barrier to initial biofilm establishment, persisting until confluent biofilm coverage of the electrode surface establishes sufficient respiratory oxygen depletion.[18,72] Along these lines, a recent study by Chen et. al revealed that planktonic growth of *C. necator* in bioelectrochemical systems could be significantly increased by displaying superoxide dismutases on the surface of the organism.[73] Process conditions were therefore modified so that *C. necator* was first grown heterotrophically on poised cathodes to increase growth rate, with conditions subsequently switched to electroautotrophic ($-45.45\ \mu A\ cm^{-2}$) once confluent coverage was achieved. Biofilm development was monitored regularly by optical coherence tomography (OCT) and used to estimate biovolume, which was subsequently normalized to the electrode surface area.

Figure 8 illustrates the resulting growth behavior. On plain graphite, an increase in biovolume was observed after the switch from heterotrophic to electroautotrophic, ultimately reaching 0.086 $mm^3\ mm^{-2}$. Growth was clearly observed not only under heterotrophic conditions but also under electroautotrophic conditions. In a parallel control experiment in which no constant negative current was applied, growth ceased once the heterotrophic carbon source and electron donor were washed out of the system (Figure 8). Under these unpolarized conditions, no external electrons were supplied at the cathode, and *C. necator* did not grow on the electrode or within the reactor channels beyond background levels. These findings confirm that electrode polarization, and thus cathodic electron supply, is essential for supporting *C. necator* growth in this system. During electroautotrophic growth a biovolume accumulation rate of $0.0076 \pm 0.0008\ mm^3\ mm^{-2}\ day^{-1}$ ($n = 3$) was measured. As mentioned earlier, the only prior study directly characterizing *C. necator* biofilm formation on cathode surfaces was reported by Bause et al.,[17] who cultivated *C. necator* in a batch stirred-tank reactor on a planar platinum cathode and assessed surface colonization by postexperiment SEM. Under their optimal condition of $-500\ \mu A\ cm^{-2}$, a maximum surface coverage of only 34.8% was achieved after 24 h, representing a sparse, uniform monolayer. Critically, this approach was end point-based and conducted under diffusion-limited, batch conditions, precluding kinetic resolution of biofilm development or assessment of convective substrate supply. By employing OCT under defined flow conditions, we provide the first continuous, noninvasive kinetic characterization of *C. necator* cathode biofilm growth, resolving biovolume accumulation over 14 days. The final biovolume of 0.086 $mm^3\ mm^{-2}$ on plain graphite demonstrates that, given appropriate inoculation conditions and controlled mass transfer, *C. necator* is capable of substantially more productive cathode colonization than the sparse colonization reported by Bause et al.[17]

3.4. Three-Dimensional Biofilm Colonization of Aerographite under Flow-Over Conditions

Evaluating biofilm growth on Aerographite is inherently complicated by the structural heterogeneity of the material: each individual sample possesses a unique pore network that gives rise to distinct local colonization patterns, as reflected in the high inter-replicate variability observed across the three Aerographite replicates in Figure 9a. All three replicates nonetheless displayed a consistent qualitative trend of increasing biovolume over time, with the heterotrophic phase yielding lower biovolume accumulation on Aerographite than on graphite during the first six days.

To enable a quantitative comparison between the two electrode materials, OCT was performed on Aerographite electrodes prior to inoculation to determine the optically accessible substratum area. The quantifiable contact surface area (calculated from OCT data) was found to be $0.18 \pm 0.033\ cm^2$ ($n = 3$) for Aerographite, approximately 60% of the 0.3 cm^2 accessible on plain graphite, reflecting the irregular surface topology of the porous material as presented to the OCT optical path. When absolute biovolume is compared on this basis, Aerographite accumulated 0.0339 $mm^3\ mm^{-2}$ after 14

https://doi.org/10.1021/acs.iecr.6c01035
Ind. Eng. Chem. Res. 2026, 65, 17018−17029

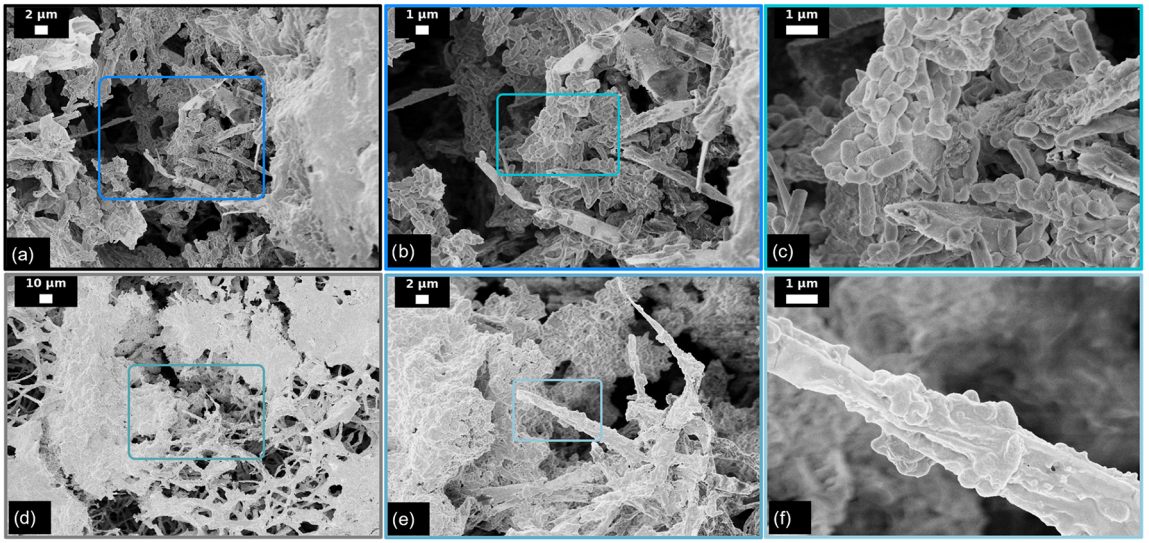

Figure 10. Side-view scanning electron micrographs of the Aerographite electrode after cutting, showing the internal *Cupriavidus necator* biofilm. (a–f) Pore network revealing *C. necator* cells colonizing both the surface and deeper bulk regions within the material's core.

days, 2.5-fold less than graphite. On this basis, Aerographite accumulated 0.0339 mm^3 mm^{-2} after 14 days, corresponding to a 2.5-fold lower absolute biovolume per projected area compared to graphite. Nevertheless, the porous nature of Aerographite means that the projected solid substratum available for biofilm colonization is intrinsically smaller than that of a poreless graphite electrode of the same geometric footprint. A direct comparison of biofilm coverage on the projected electrode surface is therefore structurally biased against Aerographite. Moreover, projected-area normalization does not capture the principal architectural advantage of Aerographite. Unlike planar graphite, where biofilm growth is intrinsically two-dimensional and capped at self-limiting thicknesses on the order of 100–150 μm (see Section 3.2.2), the hierarchical tetrapodal network of Aerographite distributes the available substratum across a three-dimensional volume that spans the full electrode thickness. This decouples biocatalyst loading from the reactor footprint: in a flow-through configuration, the same projected reactor cross-section can host substantially more active biocatalyst than is achievable on a planar surface, with corresponding gains in volumetric productivity. Consequently, when normalized to electrode mass, the parameter most relevant for scaling, Aerographite (3–12 mg cm^{-3}) supported 0.83 mm^3 mg^{-1} compared to 0.0035 mm^3 mg^{-1} for graphite, representing approximately a 237-fold mass-specific advantage on average in the samples tested in this study (depending on the electrode density in the case of Aerographite). This highlights that the ultralow density of Aerographite translates directly into superior biocatalyst loading per unit reactor weight, a key metric for scalable bioelectrochemical process design. Of note this comparison excludes biomass growth further to the center of the Aerographite electrode as shown in Figure 10.

SEM analysis after the growth experiments revealed biofilm formation not only on the external electrode surface but also within the internal pore network, as shown in Figures 9b–e and 8d–f. Cross-sections of the electrodes confirmed cell accumulation in deeper regions of the material despite the absence of flow-through conditions, indicating that passive diffusion of H_2, CO_2, and nutrients through the open tetrapodal pore network was sufficient to sustain growth beyond the directly perfused surface layer.

Inspection of the SEM images at higher magnification (Figure 9e) revealed that *C. necator* produces extracellular polymeric substance (EPS) structures that bridge between individual tetrapod arms, effectively spanning pore openings and creating multilayer biofilm patches anchored to the three-dimensional scaffold. This architectural adaptation suggests that *C. necator* actively exploits the tetrapodal geometry as a structural support for biofilm consolidation, rather than simply coating individual arm surfaces. EPS-mediated bridging between scaffold elements is expected to enhance biofilm mechanical stability under flow conditions and may facilitate the transition to a fully cohesive three-dimensional biofilm under future flow-through configurations, where higher shear forces would otherwise limit biofilm retention on planar surfaces.

4. CONCLUSION

This study provides the first kinetic characterization of *C. necator* H16 biofilm development on cathode surfaces under defined flow conditions. Direct electroautotrophic cultivation failed without prior biofilm establishment, consistent with ROS-mediated suppression of initial colonization. A biphasic cultivation strategy resolved this limitation, yielding a final biovolume of 0.086 mm^3 mm^{-2} on plain graphite after 14 days and confirming that cathodic electron supply is essential for sustained growth. These results demonstrate that *C. necator* is capable of substantially more productive electrode colonization than previously reported, provided the ROS barrier is addressed at inoculation.

Aerographite supported biomass accumulation despite its ultralow density (3–12 mg cm^{-3}), with SEM cross-sections confirming internal pore colonization even under flow-over conditions. The macropore dimensions (10–500 μm) substantially exceed documented self-limiting cathodic biofilm thicknesses, indicating that pore occlusion is unlikely even at full biofilm development, a structural advantage over conventional porous electrode materials. The transition to flow-through configurations represents the critical next engineering step, with the goal of engaging a larger fraction of the internal

https://doi.org/10.1021/acs.iecr.6c01035
Ind. Eng. Chem. Res. 2026, 65, 17018–17029

surface area electrochemically and increasing biocatalyst loading per reactor volume. The present work establishes the methodological and biological foundation for this step by demonstrating biofilm formation, internal pore accessibility, and quantifiable growth kinetics under defined flow-over conditions. The combination of Aerographite's decoupled surface-area-to-footprint ratio, membrane-free operation enabled by the aerobic hydrogenotrophic metabolism of *C. necator*, and the in situ OCT monitoring capability demonstrated here provides a coherent design basis for smart bioelectrochemical reactor systems in which electrode architecture, biofilm state, and process performance can be co-optimized in real time toward scalable and energy-efficient CO_2 valorization.

■ ASSOCIATED CONTENT

Data Availability Statement

All data collected and reported in this study have been made available under copyright at TUHH Open Research (TORE): 10.15480/882.16822

■ AUTHOR INFORMATION

Corresponding Author

Johannes Gescher − *Institute of Technical Microbiology, Hamburg University of Technology, 21073 Hamburg, Germany;* orcid.org/0000-0002-1625-8810; Email: johannes.gescher@tuhh.de

Authors

Sri Sannihita Chavali − *Institute of Technical Microbiology, Hamburg University of Technology, 21073 Hamburg, Germany;* orcid.org/0009-0008-7662-0974

Christiane Roller − *Institute of Polymer Composites, Hamburg University of Technology, 21073 Hamburg, Germany;* orcid.org/0009-0006-3350-3378

Tom Liebing − *Institute for Mechatronics in Mechanics, Hamburg University of Technology, 21073 Hamburg, Germany;* orcid.org/0000-0003-3162-4783

Jonas Lumma − *Department of Material Science, Functional Nanomaterials, Kiel University, 24143 Kiel, Germany;* orcid.org/0009-0007-6182-423X

Morten Möller − *Department of Material Science, Functional Nanomaterials, Kiel University, 24143 Kiel, Germany;* orcid.org/0009-0009-3776-4577

Rainer Adelung − *Department of Material Science, Functional Nanomaterials, Kiel University, 24143 Kiel, Germany;* orcid.org/0000-0002-2617-678X

Thorsten Alexander Kern − *Institute for Mechatronics in Mechanics, Hamburg University of Technology, 21073 Hamburg, Germany*

Miriam Edel − *Institute of Technical Microbiology, Hamburg University of Technology, 21073 Hamburg, Germany*

Bodo Fiedler − *Institute of Polymer Composites, Hamburg University of Technology, 21073 Hamburg, Germany;* orcid.org/0000-0002-2734-1353

Complete contact information is available at: https://pubs.acs.org/10.1021/acs.iecr.6c01035

Notes

The authors declare no competing financial interest.

■ ACKNOWLEDGMENTS

This project is funded by the Deutsche Forschungsgemeinschaft (DFG, German Research Foundation) − SFB 1615 − 503850735. The authors gratefully acknowledge the Electron Microscopy Unit (BeEM) at the Hamburg University of Technology (TUHH) for providing access to the scanning electron microscope (SEM). Figure 2 and the Abstract graphic were created in BioRender. Gescher, J. (2026) https://BioRender.com/jwv9vzu

■ REFERENCES

(1) Logan, B. E.; Rossi, R.; Ragab, A.; Saikaly, P. E. *Nat. Rev. Microbiol.* **2019**, *17* (5), 307−319.

(2) Bian, B.; Bajracharya, S.; Xu, J.; Pant, D.; Saikaly, P. E. *Bioresour. Technol.* **2020**, *302*, No. 122863.

(3) Reiner, J. E.; Geiger, K.; Hackbarth, M.; Fink, M.; Lapp, C. J.; Jung, T.; Dötsch, A.; Hügler, M.; Wagner, M.; Hille-Reichel, A.; Wilcke, W.; Kerzenmacher, S.; Horn, H.; Gescher, J. *ISME J.* **2020**, *14* (5), 1125−1140.

(4) Weiler, J.; Edel, M.; Gescher, J. *Annu. Rev. Chem. Biomol. Eng.* **2024**, *15* (1), 361−387.

(5) Cabau-Peinado, O.; Winkelhorst, M.; Stroek, R.; de Kat Angelino, R.; Straathof, A. J. J.; Masania, K.; Daran, J. M.; Jourdin, L. *Trends Biotechnol.* **2024**, *42* (11), 1503−1522.

(6) Salehizadeh, H.; Yan, N.; Farnood, R. *Chem. Eng. J.* **2020**, *390*, No. 124584.

(7) Pillot, G.; Sunny, S.; Comes, V.; Kerzenmacher, S. *Bioresour. Technol. Rep.* **2022**, *17*, No. 100949.

(8) Pous, N.; Balaguer, M. D.; Matassa, S.; Chiluiza-Ramos, P.; Bañeras, L.; Puig, S. *Bioresour. Technol. Rep.* **2022**, *18*, No. 101010.

(9) Eberhard Reiner, J.; Korth, B.; Edel, M. *ChemElectroChem* **2024**, *11* (20), No. e202400397, DOI: 10.1002/celc.202400397.

(10) Marcellin, E.; Angenent, L. T.; Nielsen, L. K.; Molitor, B. *Curr. Opin. Biotechnol.* **2022**, *76*, No. 102723.

(11) Mishra, A.; Ntihuga, J. N.; Molitor, B.; Angenent, L. T. *Joule* **2020**, *4* (6), 1142−1147.

(12) Rominger, L.; Hackbarth, M.; Jung, T.; Scherzinger, M.; Rosa, L. F. M.; Horn, H.; Kaltschmitt, M.; Picioreanu, C.; Gescher, J. *Trends Biotechnol.* **2025**, *43* (3), 673−695.

(13) Hackbarth, M.; Jung, T.; Reiner, J. E.; Gescher, J.; Horn, H.; Hille-Reichel, A.; Wagner, M. *Chem. Eng. J.* **2020**, *390*, No. 124604.

(14) Jung, T.; Hackbarth, M.; Horn, H.; Gescher, J. *Microorganisms* **2021**, *9* (1), No. 77.

(15) Blankenship, R. E.; Tiede, D. M.; Barber, J.; Brudvig, G. W.; Fleming, G.; Ghirardi, M.; Gunner, M. R.; Junge, W.; Kramer, D. M.; Melis, A.; Moore, T. A.; Moser, C. C.; Nocera, D. G.; Nozik, A. J.; Ort, D. R.; Parson, W. W.; Prince, R. C.; Sayre, R. T. *Science* **2011**, *332* (6031), 805−809.

(16) Prévoteau, A.; Carvajal-Arroyo, J. M.; Ganigué, R.; Rabaey, K. *Curr. Opin. Biotechnol.* **2020**, *62*, 48−57.

(17) Bause, S.; Decker, M.; Neubauer, P.; Vonau, W. *Chem. Pap* **2018**, *72* (5), 1205−1211.

(18) Tian, J.-H.; Lacroix, R.; Quéméner, E.D.-L.; Bureau, C.; Midoux, C.; Bouchez, T. 2019 DOI: 10.1101/609909.

(19) Jourdin, L.; Freguia, S.; Flexer, V.; Keller, J. *Environ. Sci. Technol.* **2016**, *50* (4), 1982−1989.

(20) Vassilev, I.; Dessì, P.; Puig, S.; Kokko, M. *Bioresour. Technol.* **2022**, *348*, No. 126788.

(21) Jourdin, L.; Freguia, S.; Donose, B. C.; Chen, J.; Wallace, G. G.; Keller, J.; Flexer, V. *J. Mater. Chem. A* **2014**, *2* (32), 13093−13102.

(22) Flexer, V.; Jourdin, L. *Acc. Chem. Res.* **2020**, *53* (2), 311−321.

(23) Jourdin, L.; Grieger, T.; Monetti, J.; Flexer, V.; Freguia, S.; Lu, Y.; Chen, J.; Romano, M.; Wallace, G. G.; Keller, J. *Environ. Sci. Technol.* **2015**, *49* (22), 13566−13574.

(24) Jourdin, L. *Microbial Electrosynthesis from Carbon Dioxide: Performance Enhancement and Elucidation of Mechanisms*; The University of Queensland, 2015.

(25) Averbukh, M.; Lugovskoy, S.; Kossenko, A. *Proceedings of the Tenth International Conference on Material Technologies and Modeling (MMT-2018)*; Ariel: Israel, 2018; pp 148−157.
(26) Banerjee, R.; Bevilacqua, N.; Mohseninia, A.; Wiedemann, B.; Wilhelm, F.; Scholta, J.; Zeis, R. *J. Energy Storage* **2019**, *26*, No. 100997.
(27) Kossenko, A.; Lugovskoy, S.; Averbukh, M. *Materials* **2018**, *11* (4), 650.
(28) Sleutels, T.H.J.A.; Lodder, R.; Hamelers, H. V. M.; Buisman, C. J. N. *Int. J. Hydrogen Energy* **2009**, *34* (24), 9655−9661.
(29) Caizán-Juanarena, L.; Sleutels, T.; Kokko, M.; Berenguer, R.; ter Heijne, A. Microbial Electrochemical Technologies. In *Emerging Trends and Advances*; Elsevier, 2024; pp 425−478.
(30) Yaqoob, A. A.; Mohamad Ibrahim, M. N.; Rafatullah, M.; Chua, Y. S.; Ahmad, A.; Umar, K. *Materials* **2020**, *13* (9), 2078.
(31) Mecklenburg, M.; Schuchardt, A.; Mishra, Y. K.; Kaps, S.; Adelung, R.; Lotnyk, A.; Kienle, L.; Schulte, K. *Adv. Mater.* **2012**, *24* (26), 3486−3490.
(32) Garlof, S.; Mecklenburg, M.; Smazna, D.; Mishra, Y. K.; Adelung, R.; Schulte, K.; Fiedler, B. *Carbon* **2017**, *111*, 103−112.
(33) Garlof, S.; Fiedler, B. *Nanocomposites* **2016**, *2* (4), 153−161.
(34) Frackowiak, E.; Béguin, F. *Carbon* **2001**, *39* (6), 937−950.
(35) Simon, P.; Gogotsi, Y. *Nat. Mater.* **2008**, *7* (11), 845−854.
(36) Biener, J.; Stadermann, M.; Suss, M.; Worsley, M. A.; Biener, M. M.; Rose, K. A.; Baumann, T. F. *Energy Environ. Sci.* **2011**, *4* (3), 656.
(37) Moreno-Castilla, C.; Maldonado-Hódar, F. J. *Carbon* **2005**, *43* (3), 455−465.
(38) Lupan, O.; Postica, V.; Mecklenburg, M.; Schulte, K.; Mishra, Y. K.; Fiedler, B.; Adelung, R. *J. Mater. Chem. A Mater.* **2016**, *4* (42), 16723−16730.
(39) Pekala, R. W.; Kong, F. M. 1988.
(40) Bryning, M. B.; Milkie, D. E.; Islam, M. F.; Hough, L. A.; Kikkawa, J. M.; Yodh, A. G. *Adv. Mater.* **2007**, *19* (5), 661−664.
(41) Gui, X.; Wei, J.; Wang, K.; Cao, A.; Zhu, H.; Jia, Y.; Shu, Q.; Wu, D. *Adv. Mater.* **2010**, *22* (5), 617−621.
(42) Zou, J.; Liu, J.; Karakoti, A. S.; Kumar, A.; Joung, D.; Li, Q.; Khondaker, S. I.; Seal, S.; Zhai, L. *ACS Nano* **2010**, *4* (12), 7293−7302.
(43) Worsley, M. A.; Pauzauskie, P. J.; Olson, T. Y.; Biener, J.; Satcher, J. H.; Baumann, T. F. *J. Am. Chem. Soc.* **2010**, *132* (40), 14067−14069.
(44) Zhang, Q.; Zhang, F.; Medarametla, S. P.; Li, H.; Zhou, C.; Lin, D. *Small* **2016**, *12* (13), 1702−1708.
(45) Liu, F.; Seo, T. S. *Adv. Funct. Mater.* **2010**, *20* (12), 1930−1936.
(46) Lamprecht, C.; Taale, M.; Paulowicz, I.; Westerhaus, H.; Grabosch, C.; Schuchardt, A.; Mecklenburg, M.; Böttner, M.; Lucius, R.; Schulte, K.; Adelung, R.; Selhuber-Unkel, C. *ACS Appl. Mater. Interfaces* **2016**, *8* (24), 14980−14985.
(47) Jourdin, L.; Burdyny, T. *Trends Biotechnol.* **2021**, *39* (4), 359−369.
(48) Lu, J.; Brigham, C. J.; Li, S.; Sinskey, A. J. *Biotechnology for Biofuel Production and Optimization*; Elsevier, 2016; pp 325−351.
(49) Windhorst, C.; Gescher, J. *Biotechnol. Biofuels* **2019**, *12* (1), No. 163, DOI: 10.1186/s13068-019-1512-x.
(50) Klein, E.; Wurst, R.; Rehnlund, D.; Gescher, J. *Biofilm* **2024**, *7*, No. 100193, DOI: 10.1016/j.bioflm.2024.100193.
(51) Mishra, Y. K.; Modi, G.; Cretu, V.; Postica, V.; Lupan, O.; Reimer, T.; Paulowicz, I.; Hrkac, V.; Benecke, W.; Kienle, L.; Adelung, R. *ACS Appl. Mater. Interfaces* **2015**, *7* (26), 14303−14316.
(52) Mishra, Y. K.; Kaps, S.; Schuchardt, A.; Paulowicz, I.; Jin, X.; Gedamu, D.; Freitag, S.; Claus, M.; Wille, S.; Kovalev, A.; Gorb, S. N.; Adelung, R. *Part. Part. Syst. Charact.* **2013**, *30* (9), 775−783.
(53) Rasch, F.; Schütt, F.; Saure, L. M.; Kaps, S.; Strobel, J.; Polonskyi, O.; Nia, A. S.; Lohe, M. R.; Mishra, Y. K.; Faupel, F.; Kienle, L.; Feng, X.; Adelung, R. *ACS Appl. Mater. Interfaces* **2019**, *11* (47), 44652−44663.
(54) Beisch, H.; Fiedler, B. *Synthesis and Applications of Nanocarbons*; Wiley, 2020; pp 247−274.
(55) Sydow, A.; Krieg, T.; Ulber, R.; Holtmann, D. *Eng. Life Sci.* **2017**, *17* (7), 781−791.
(56) Weiler, J. R.; Jürgensen, N.; Cornejo Infante, M.; Knoll, M. T.; Gescher, J. *Biotechnol. Biofuels Bioprod.* **2024**, *17* (1), 108.
(57) Roessler, B.; Off, S.; Arendt, O.; Gescher, J. *Bioresour. Technol. Rep.* **2024**, *27*, No. 101875.
(58) Esmizadeh, E.; Tzoganakis, C.; Mekonnen, T. H. *Polymers* **2020**, *12* (8), 1627.
(59) Farivar, F.; Lay Yap, P.; Karunagaran, R. U.; Losic, D. *C* **2021**, *7* (2), No. 41.
(60) Jiang, W.; Nadeau, G.; Zaghib, K.; Kinoshita, K. *Thermochim. Acta* **2000**, *351* (1−2), 85−93.
(61) Wurst, R.; Klein, E.; Gescher, J. *Biofilm* **2024**, *8*, No. 100226.
(62) Bard, A. J.; Mirkin, M. V. *Scanning Electrochemical Microscopy*; CRC Press, 2001.
(63) Elgrishi, N.; Rountree, K. J.; McCarthy, B. D.; Rountree, E. S.; Eisenhart, T. T.; Dempsey, J. L. *J. Chem. Educ.* **2018**, *95* (2), 197−206.
(64) Sleutels, T.H.J.A.; Hamelers, H. V. M.; Rozendal, R. A.; Buisman, C. J. N. *Int. J. Hydrogen Energy* **2009**, *34* (9), 3612−3620.
(65) Veys, E.; Makower, L.; Williamson, M.; Saure, L. M.; Adelung, R.; Schütt, F.; Pugno, N. M.; Marrow, T. J. *Scr. Mater.* **2023**, *224*, No. 115153.
(66) Marx, J. *Fundamentals of the growth mechanism, tailored properties and applications of 3D hollow carbon foams*; Technische Universität: Hamburg, 2019.
(67) Harrington, T. D.; Babauta, J. T.; Davenport, E. K.; Renslow, R. S.; Beyenal, H. *Biotechnol. Bioeng.* **2015**, *112* (5), 858−866.
(68) Netsch, A.; Latussek, I.; Horn, H.; Wagner, M. *Biotechnol. Bioeng.* **2025**, *122* (8), 2049−2062.
(69) Reiner, J. E.; Jung, T.; Lapp, C. J.; Siedler, M.; Bunk, B.; Overmann, J.; Gescher, J. *Int. J. Syst. Evol. Microbiol.* **2018**, *68* (12), 3735−3740.
(70) Ishizaki, A.; Tanaka, K.; Taga, N. *Appl. Microbiol. Biotechnol.* **2001**, *57* (1−2), 6−12.
(71) Torella, J. P.; Gagliardi, C. J.; Chen, J. S.; Bediako, D. K.; Colón, B.; Way, J. C.; Silver, P. A.; Nocera, D. G. *Proc. Natl. Acad. Sci.* **2015**, *112* (8), 2337−2342.
(72) Bause, S.; Decker, M.; Neubauer, P.; Vonau, W. *Chem. Pap.* **2018**, *72* (5), 1205−1211.
(73) Chen, K.; Ma, C.; Cheng, X.; Wang, Y.; Guo, K.; Wu, R.; Zhu, Z. *Bioresour. Bioprocess.* **2023**, *10* (1), No. 36.